Bauer, D., Chaves, H. & Arcoumanis, C. (2012). Measurements of void fraction distribution in cavitating pipe flow using x-ray CT. Measurement Science and Technology, 23(5), 055302.. doi: 10.1088/0957-0233/23/5/055302

CITY UNIVERSITY LONDON

EST 1894

City Research Online

Measurements of void fraction distribution in cavitating pipe flow using x-ray CT

D Bauer[1,3]**, H Chaves**[1] **and C Arcoumanis**[2]

[1] Institute of Mechanics and Fluid Dynamics, TU Bergakademie Freiberg, Lampadiusstr. 4, D-09596 Freiberg, Germany
[2] Centre for Energy and the Environment, School of Engineering and Mathematical Sciences, City University, London, UK

E-mail: Daniel.Bauer@imfd.tu-freiberg.de

Abstract
Measuring the void fraction distribution is still one of the greatest challenges in cavitation research. In this paper, a measurement technique for the quantitative void fraction characterization in a cavitating pipe flow is presented. While it is almost impossible to visualize the inside of the cavitation region with visible light, it is shown that with x-ray computed tomography (CT) it is possible to capture the time-averaged void fraction distribution in a quasi-steady pipe flow. Different types of cavitation have been investigated including cloud-like cavitation, bubble cavitation and film cavitation at very high flow rates. A specially designed nozzle was employed to induce very stable quasi-steady cavitation. The obtained results demonstrate the advantages of the measurement technique compared to other ones; for example, structures were observed inside the cavitation region that could not be visualized by photographic images. Furthermore, photographic images and pressure measurements were used to allow comparisons to be made and to prove the superiority of the CT measurement technique.

1. Introduction

Cavitation plays an important role in different engineering applications such as fuel injection nozzles, ship propellers and fuel pumps. In the first example, cavitation can cause instabilities and flow rate fluctuations that may lead to improved vaporization of the fuel. At the same time, cavitation can cause damage in high pressure pumps of the injection system. This damage is caused by the collapse of vapor bubbles close to rigid walls and is known as cavitation erosion. The same phenomenon is more common in ship propellers and certain types of pumps. This type of corrosion could also be a problem with artificial heart flaps [8] and is part

of ongoing research [7]. In this work, the emphasis is on pipe flows. Although numerical investigations of cavitation research have become more and more sophisticated [5] within the past two decades, there is still a need for carefully designed experiments, either, for example, for model validation or for investigating different forms of cavitation. Chaves *et al* [9] have described the so-called pig tail cavitation observed in a transparent real size VCO[4] nozzle with a transparent needle. So, it was possible to take images from the direction of the hole's exit and observe this type of cavitation [9]. However, even with such a highly sophisticated experimental technique, it proved very difficult to measure the actual void fraction. The observation of pig tail cavitation proved that flows with cavitation can be extremely three-dimensional.

---

[4] Valve-covered orifice.

There is therefore a need for a measurement technique capable of measuring such structures. Since visible light is scattered at the vapor–liquid boundary layer, harder radiation such as x-rays is needed for these measurements which are not scattered at the gas–liquid interface. Over the past few years, much effort has been put into this field of cavitation research. By examining a cavitating flow with x-rays, a quantitative information about the void fraction can be obtained [4]. However, by using standard x-ray application, only integral information about the void fraction within the area of interest can be derived. It is hardly possible to gather information on the structures inside the cavitation.

It is possible to use high speed imaging [11] or double imaging with x-rays as a light sources [12]. A high-speed camera behind the x-ray detector allows us to study the dynamic processes of the growing and collapsing of cavitation bubbles [1]. For double imaging, either a double-shutter camera is used behind the detector or a shutter for the x-ray beam source is used to generate double images with a fixed time interval. The images are recorded with a high-speed camera. This setup is similar to the PIV (particle image velocimetry) technique; however, no tracer particles are added to the fluid; instead, the cavitation bubbles themselves or bigger cavitation structures are correlated by PIV algorithms [6]. For these experiments, shutter times in the order of a few microseconds are needed. This method is a very good approach to study the velocity fields outside the cavitation area as well as the interaction between bubbles and the liquid flow. However, even in this case, it is not possible to get information from the inner cavitation area.

This fact has prompted the idea to use an x-ray computed tomography (CT) scanner to measure the void fraction distribution of a cavitating pipe flow. The advantage of the CT is that it does not only measure the spatial average of the void fraction, like it would be on a normal x-ray, but the void fraction distribution along a cross section of the pipe. In the field of hydrology, CT has been used to characterize phase distribution of water, air and soil as well as the pore geometry in porous media [13].

In the next section, an approach to measuring the void fraction and void fraction distribution in cavitating pipe flows will be presented using a standard medical CT system. The results are compared with other measurement techniques such as pressure measurements and standard digital imaging.

2. Measurement instrumentation

2.1. Principles of x-ray computed tomography

X-ray computed tomography is an imaging technique that uses x-rays to scan the cross section of a test object (see figure 1). The basic idea for generating an image with CT goes back to the beginning of the 20th century when the mathematician Radon showed [10] that a property of a 2D object can be exactly described if an infinite number of line integrals about the property from different directions are defined. Such line integrals could be directly measured if radiation, which is absorbed by matter, is detected behind the object. The amount
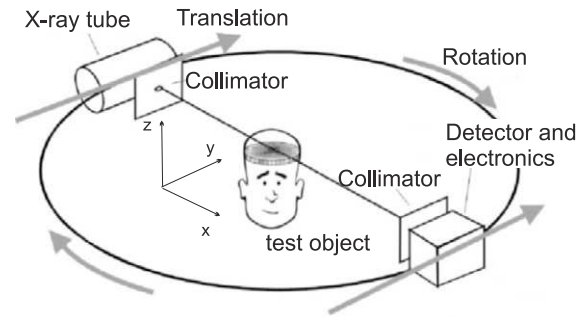

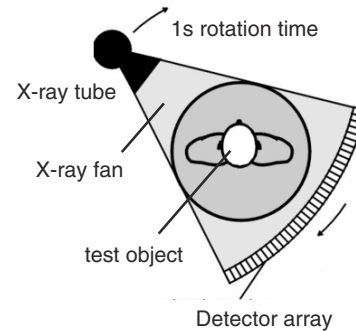**Figure 1.** Basic principle of computed tomography from [14].

Figure 2. Basic principle of modern computed tomography [14].

of radiation reaching the detector represents the line integral of the attenuation coefficients along the path of the beam inside the object. Depending on the type of material, the radiation could be visible light, microwaves, radio waves or radioactive radiation like x-rays. The advantage of x-rays is the hardness of the radiation which is ideal for the present application. Visible light, for example, would be scattered at the boundary layer between vapor and liquid. On the other hand, the x-ray beam is weakened by the matter inside the object; since the object is not homogeneous, the attenuation coefficient does not remain constant along the path and depends on the density of the material.

The basic idea of CT is to create an image of the interior of the object using a large number of line integrals over the attenuation coefficients. It should be noted that the x-ray beam is not 2D but has an extension in the third dimension, i.e. the absorption of the beam takes place within a flat 3D slice of the test object. To create a higher number of line integrals instantaneously, an x-ray fan and a detector array are used. The fan is generated in an x-ray tube and shaped with a collimator (lead plate with a slit) in such a way that the resulting x-ray fan is flat.

The number of detectors within the detector array behind the object represents the number of line integrals at a fixed angle (see figure 2). Tube and array are rotating simultaneously around the object. All intensity values measured instantaneously at a fixed angle are called a projection. For symmetry reasons, the projections are taken between angles $0°–180°$.

The attenuation coefficients within a slice of the test object can be reconstructed from the projections of this slice. The result of the reconstruction process is a gray scale image that

shows the attenuation coefficients inside the slice. Since a slice of the object is not 2D, each pixel inside the image represents a so-called voxel, which is a 3D pixel. The brighter the voxel, the higher the attenuation coefficient. Within the image, the attenuation coefficient is displayed in the so-called Hounsfield[5] units (HU). This value is indirect and is calculated by

$$\text{HU} = \frac{\mu - \mu_{\text{H}_2\text{O}}}{\mu_{\text{H}_2\text{O}}} \times 1000. \qquad (1)$$

Here, μ represents a variable attenuation coefficient and $\mu_{\text{H}_2\text{O}}$ is the attenuation coefficient of water. As one can derive from equation (1), the HU value of water is 0. Because of that definition of HU, medical CT systems are calibrated with pure water. Since $\mu \approx 0$ for gases, the corresponding HU is about -1000. Within the images, these values are shifted by 1000 such that the nominal gray value of air is 0 and that of water is 1000. It will be shown later that the gray value of 1000 for water has an error about 2.4%.

In addition, it has to be mentioned that the thickness of a voxel in the z-direction (perpendicular to the x-ray fan) is ten times higher than the dimension of the voxel in the x- and y-directions (in the fan's plane). To reconstruct the image correctly, each projection has to be multiplied with a so-called convolution kernel (figure 3). Without it, the picture appears blurred and very soft, while, with the convolution kernel, its sharpness can be adjusted from sharp to soft.

Problems occur if objects with a high attenuation coefficient are located inside the x-ray fan, which results in a wrong reconstruction of the attenuation coefficients. In the pictures, these errors occur as shadows, so-called artifacts. This means that for the construction of an experimental setup, special care has to be taken that no materials with high absorption rates are within the test section. Another problem may occur if the test object is moving. This phenomenon is called motion artifact and leads to a blurred image, in which it is hardly possible to see sharp contours. One can argue that a flow with cavitation is in motion all the time. However, this means that we may not be able to measure certain structures. What can be measured is the time-averaged void fraction over one rotation cycle within the whole cross section. It will be demonstrated in sections 4.2 and 4.3 that accurate measurements of the spatial-averaged void fraction are possible. Further, it will also be shown in section 4.4 that inside the cavitation area, fixed regions of cavitation are visible within the CT images. As a convolution kernel, we have chosen a soft one, since we are only interested in time-averaged values so that the boundaries of the cavitation areas are smoother.

2.1.1. The CT system.

The CT system used in this project is a Philips MX 8000 IDT (see figure 4) which has not just one detector array but 16; this allows 16 slices with a thickness of 0.75 mm to be taken within one measurement cycle. Each detector array has 1024 detectors. For better image quality we combined every second array, so that 8 slices were measured in one rotation cycle; the frequency of rotation was 1 Hz. With the Philips CT system, it was also possible to use a special mode, the so-called spiral mode, when the motorized
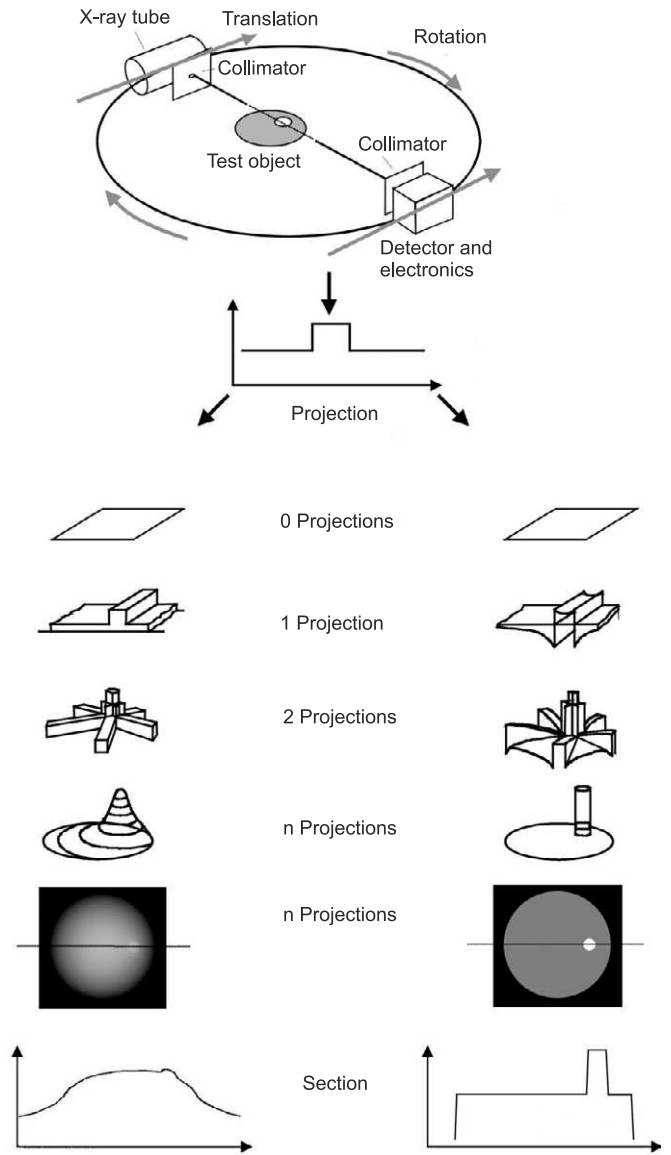
---

5 G N Hounsfield (1919–2004), inventor of the first medical CT.

Figure 3. Effects of the convolution kernel, from [14].

platform is moving with constant speed while the tube and array are rotating with a constant frequency, thus reducing the measurement time for the whole object. However, this requires an additional interpolation procedure which precluded the use of this measurement mode for quantitative measurements.

2.2. Photographic images

A digital CMOS camera and a flashlight were used to take photographic images of cavitation. Special care was taken to diffuse the flashlight through a diffusing screen in order to reduce reflection on the outside of the nozzle. The camera and flashlight were synchronized by a trigger box. The schematics of the measurement setup for the digital images can be seen in figure 5. Important for the image quality are very short exposure times which were in the order of a few microseconds.
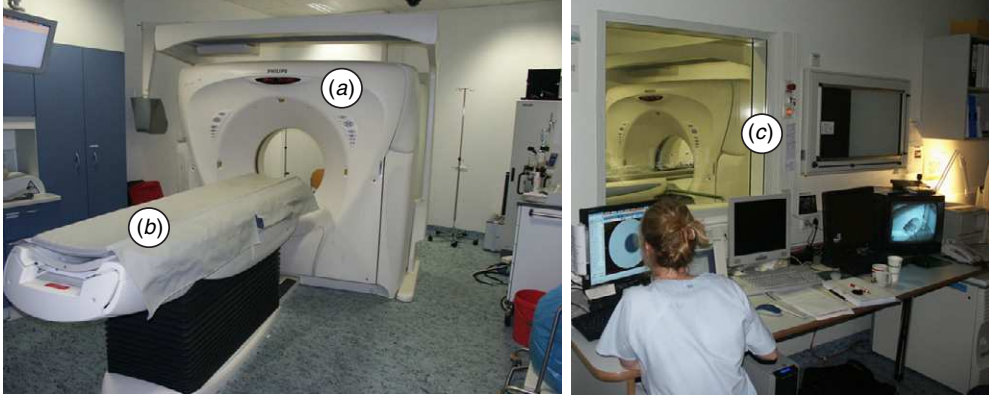
Figure 4. The CT system used: (*a*) gantry, (*b*) motorized platform, (*c*) control room.
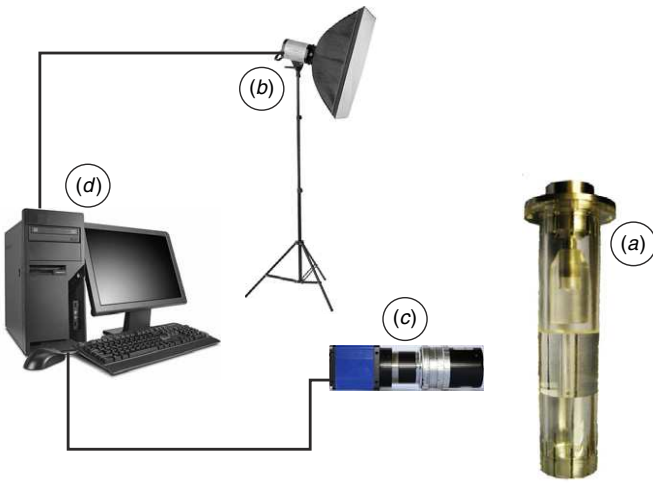

Figure 5. Experimental setup for taking photographic images: (*a*) nozzle, (*b*) flashlight with diffusing screen, (*c*) camera, (*d*) PC for image acquisition, synchronization and data storage.

2.3. Pressure measurements

Within this study, we have measured the static pressure inside the cavitation channel. Furthermore, we have measured the static pressure before (p_1) and after (p_2) the cavitation channel in order to calculate the cavitation number C_n [3], which is defined as

$$C_n = \frac{p_1 - p_2}{p_2 - p_V}, \qquad (2)$$

where p_V is the vapor pressure of water. Since $p_V \ll p_2$, equation (2) can be well approximated as

$$C_n = \frac{p_1 - p_2}{p_2}. \qquad (3)$$

The pressure was measured via pressure tappings and a water-filled, small, flexible pipe with an inner diameter of 2 mm. The pressure gauge was a Digitron 2025P with an uncertainty of 1%. With this instrument absolute values of the pressure with a range of 0−2000 mbar can be measured. From each measurement position, the small pipes end in a hydraulic switch. The pressure gauge is connected to the exit of the switch. Thereby, the pressure at each measurement position can be obtained independently. Since the flow is quasi-steady, this gauge is adequate for the present investigation. For higher

pressures, an analog manometer with an uncertainty of 1% was used. This instrument measures absolute values as well. The measurement range was 0−2000 mbar. The uncertainty in the cavitation number was 2%.

3. Experimental setup

The nozzle where cavitation was generated is shown in figure 6; it is made of Perspex®. The absorption rate of this material is slightly higher than that of water, so it is very easy to distinguish between Perspex® and the fluid flow within the nozzle in the CT images. As mentioned previously, the HU value of water is 1000 and that of Perspex® is 1180.

The basic idea to generate quasi-steady cavitation is illustrated in the nozzle cross section in figure 7. Water flows from the pipe into the nozzle entrance and is guided through three slits towards the outside between an aluminum cylinder and the outer shell of the nozzle. The cylinder has no sharp edges at the end in order to avoid flow separation at this point. The flow is then guided towards the direction of the cavitation channel.

The distance (X^*) between the front of the cylinder and the entrance to the cavitation channel (20 mm in diameter) can be adjusted at 16, 11, 6 and 2 mm. The closer the cylinder is to the cavitation channel, the higher is the entrance velocity. This, in addition to the abrupt 90° flow turn, causes a very low static pressure at the entrance of the channel resulting in cavitation. After the cavitation channel, the diameter of the nozzle increases to 70 mm in order to raise the pressure and cause the collapse of cavitation. Special care was taken to ensure that no metal parts (which would cause artifacts) were within the x-ray beam. We used two similar Perspex models for the different measurements. The one used for CT measurements and photographic images had a perfect shell around the cavitation channel in order to prevent artifacts in the CT images and optical disturbances in the photographs. The second model was used for pressure measurements inside the cavitation channel. Therefore, holes for pressure tappings had to be drilled within the shell. The pressure was measured at six positions in the cavitation channel; namely at 5 mm, 12 mm, 20 mm, 27mm, 55 mm and 95 mm relative to the cavitation channel entrance (see figure 7). The junctions for
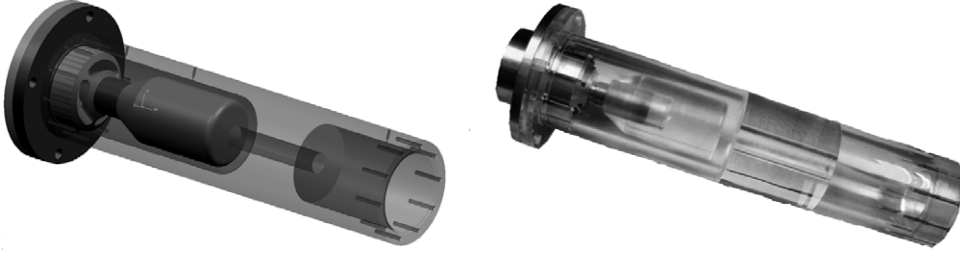
Figure 6. Nozzle design to induce cavitation: CAD model (left), manufactured nozzle (right).
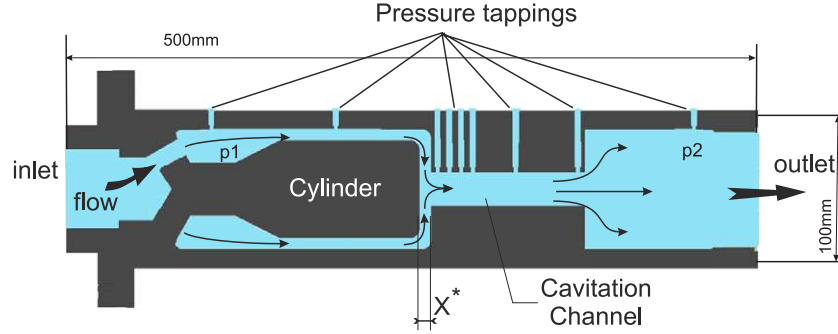

Figure 7. Basic design to create quasi-steady cavitation: cross section of the cavitating nozzle.

the gauge meter were realized with small metal tubes which explains why this model cannot be used for CT measurements.

The nozzle has been integrated into a mobile flow test rig (figure 8). The mobility of the test rig was necessary to allow measurements in a medical CT. The maximum flow rate $\dot{V}$ depends on the distance X^* and varied between $\dot{V} = 4.0\,1\,\mathrm{s}^{-1}$ for $X^* = 16\,\mathrm{mm}$ and $\dot{V} = 2.7\,1\,\mathrm{s}^{-1}$ for $X^* = 2\,\mathrm{mm}$. In section 4, we only present the case $X^* = 6\,\mathrm{mm}$. Using the tee branch and two valves (see figure 8(c)), the flow rate could be adjusted continuously from 0 to the maximum. Within the main circuit, the flow passes a 3.2 cm tube whereas the secondary flow is guided through a 2.5 cm bypass back into the tank. The advantage of this solution is that the static pressure inside the piping is relatively low compared to a one-valve solution. From the nozzle, the water flows back into the tank via a 5.1 cm pipe. The flow rate was measured in the 3.2 cm main pipe. This test rig was used for both laboratory and hospital measurements.

4. Results

With the nozzle described in section 3, it is possible to recreate a large range of cavitation types such as cloud-like cavitation, bubble cavitation and even film cavitation at higher flow rates (see figure 9). An overview of these cavitation types can be found e.g. in Brennen [2].

All experimental conditions are summarized in table A1 (appendix). Every case was investigated by means of CT, photographic images and pressure measurements. Within the next sections, only the 6 mm case is presented in detail; the other three distances X^* result in similar cavitation structures but at different flow rates.

4.1. Cavitation types and corresponding pressure curves

In figure 9, various cavitation structures can be seen.

Up to a cavitation number of $C_n = 0.75$, no cavitation structures can be observed (figure 10(a)). The first cavitation structure in the form of light cloud-type cavitation occurs at cavitation numbers of $0.75 < C_n < 1$ (figure 10(b)). It is characterized by small cavitation structures including some tiny bubbles. The next stage is a combination between bubble cavitation and cloud-like cavitation (figure 10(c)) which starts at cavitation numbers around $C_n = 1$. Larger bubbles are evident at this stage at the entrance of the cavitation channel where the pressure is very low. Further downstream, the pressure rises again and the bubbles become smaller while cavitation changes back into cloud-like cavitation.

At $C_n = 1.5$, the liquid starts to separate completely from the wall (figure 10(d)). This stage is known as film cavitation and there is only vapor between the water and the wall. The static pressure drops below 60 mbar (figures 10(c) and (d)) in the areas where film cavitation occurs. Later, the pressure rises again and cavitation changes first into bubble cavitation, and then into cloud-like cavitation before collapsing at the exit of the cavitation channel. A few small structures leaving the channel and collapsing further downstream are observed. In the case of film cavitation (figures 10(c) and (d)), the pressure at the wall drops down to levels close to the vapor pressure of water. Dissolved gases in the water like oxygen or carbon dioxide are the reason why the pressure is slightly higher than the vapor pressure. For the cases of figures 10(a) and (b), the pressure in the cavitation region also drops down to the vapor pressure of the liquid. The lowest pressure for these cases would be expected at the sharp edges at the entrance of the cavitation channel, where pressure measurements were no longer possible.
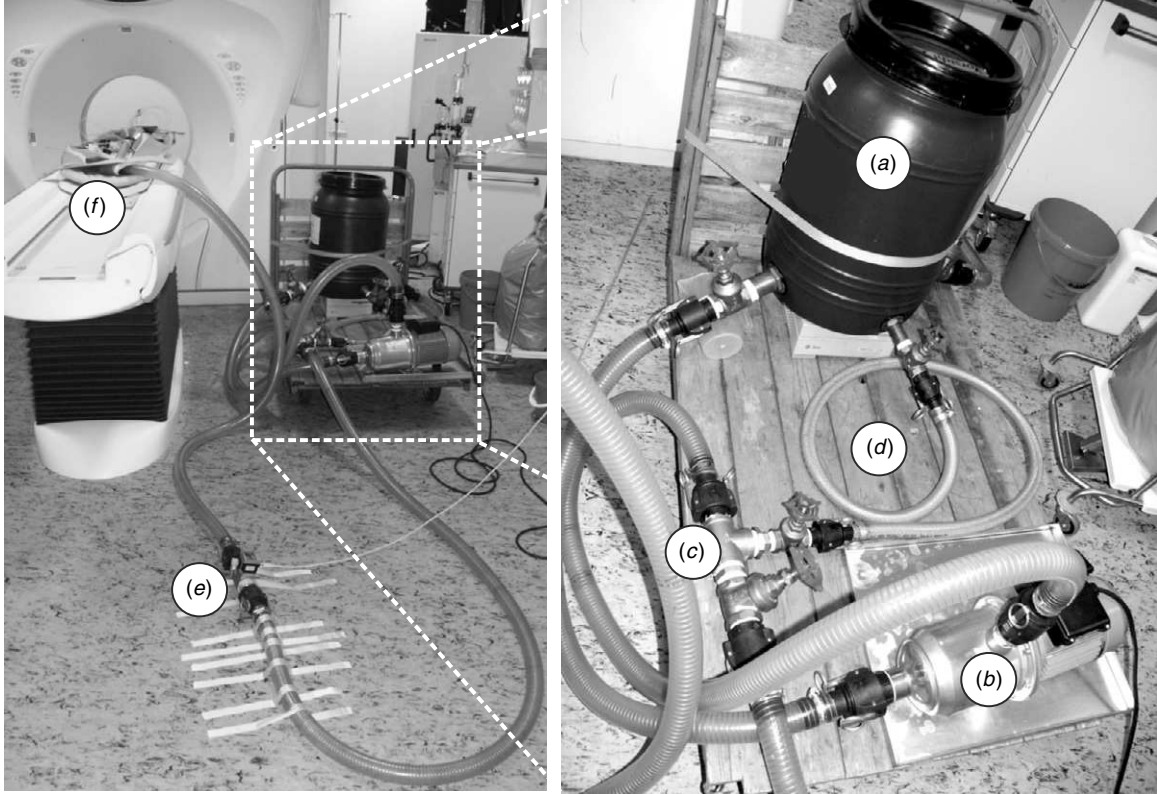
Figure 8. Mobile test rig: (*a*) tank, (*b*) pump, (*c*) tee branch with two valves, (*d*) bypass, (*e*) main pipe with flow meter, (*f*) nozzle.
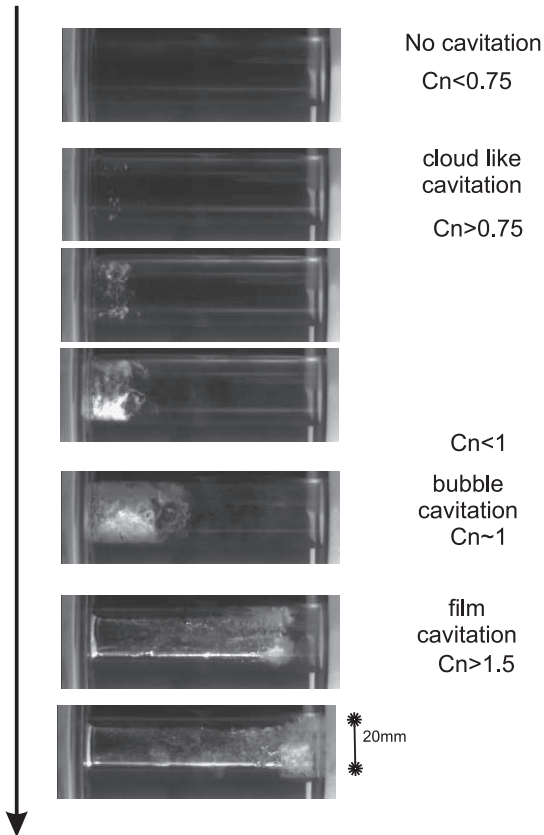

Figure 9. Types of cavitation as evidenced through photographic images.

4.2. CT calibration

In this section, the measured HU values for air and water are presented. To measure these values, the nozzle was filled with air and later with water. For each case, the obtained CT images are shown in figure 11. From these images, the averaged measured HU values (42 for air and 1024 for water) were calculated by summing up every gray value within the channel and dividing it by the number of pixels. This yields a relative error of 4.2% for air and 2.4% for water which are considered acceptable.

If the gray value of water is 1000 and the one of air is 0, a value α can be defined that represents the relative amount of water within one voxel and is given by

$$\alpha = \frac{HU}{10}. \tag{4}$$

4.3. Spatial averaged void fraction

The results for the spatial-averaged void fraction in the cavitation channel are presented in figure 12; the averaged values are calculated from the CT images. The HU values inside the channel are averaged and divided by 10, which provides the averaged amount of water α^* ($\alpha^* = \bar{\alpha}$, given in %) within the investigated slice. The results for each slice are plotted over the distance z. For each case, photographic images are included for direct comparison.

In figure 12(*a*), the case of light cloud-like cavitation ($C_n = 0.95$) is presented. As can be seen from the plot, the lowest value of α^* close to the entrance is 97% which implies that the fluid is nearly 100% water. At $z = 20$ mm
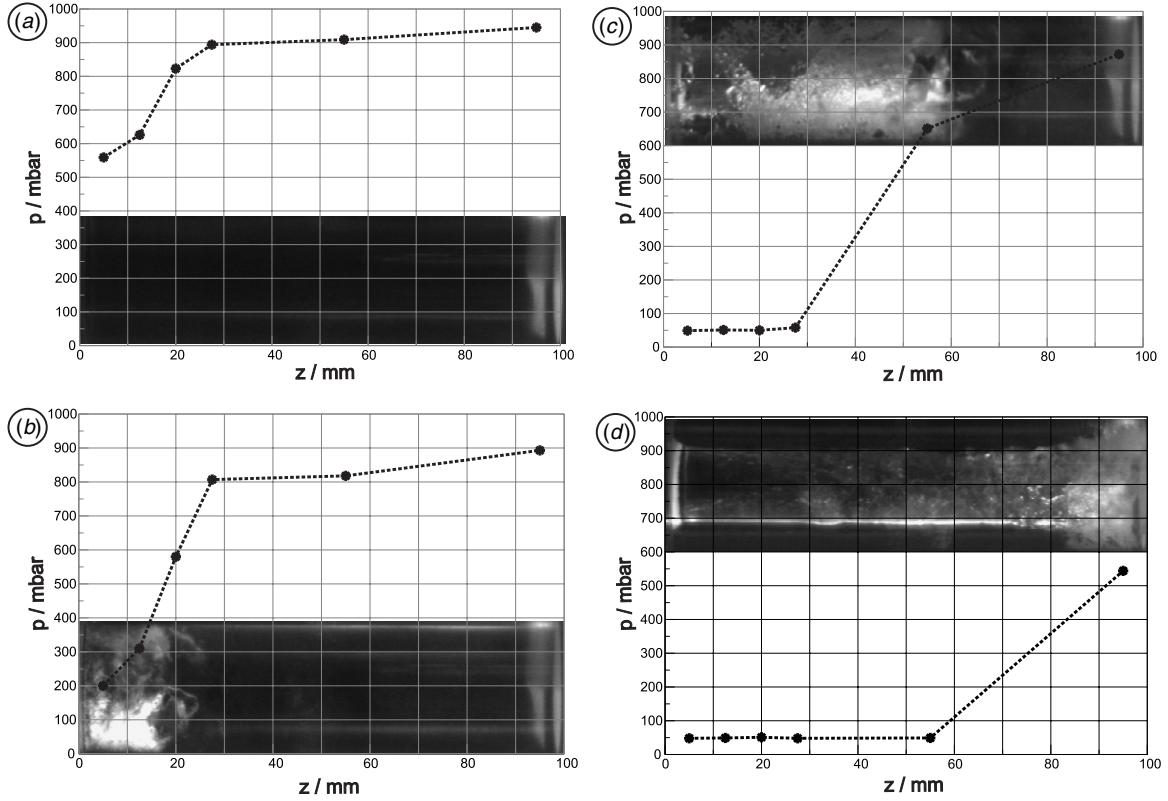
Figure 10. Pressure measurements at (*a*) $C_n = 0.5$, (*b*) $C_n = 0.95$, (*c*) $C_n = 1.1$, (*d*) $C_n = 1.5$; the dashed lines are only integrated for better visualization of the pressure values but do not represent physical values between the measurement points.
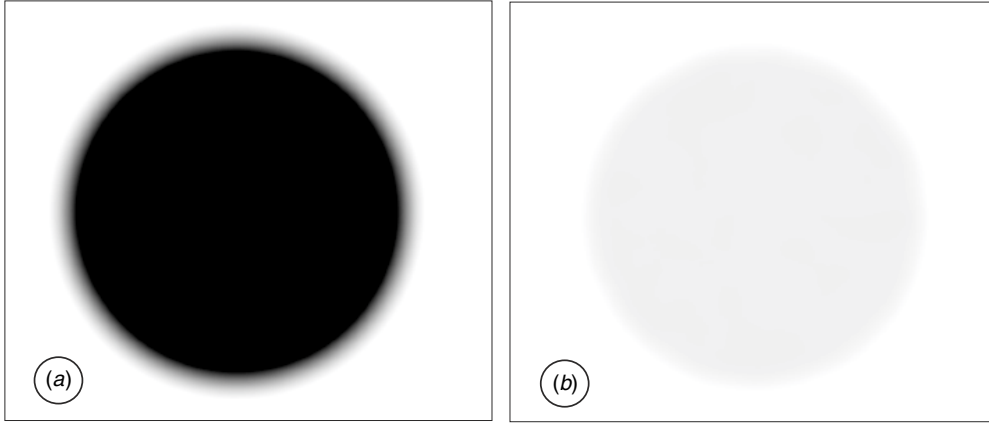

Figure 11. (*a*) CT image for air; averaged measured HU value is 42. (*b*) CT image for pure water; averaged measured HU value is 1024.

downstream from the entrance, light cloud-like cavitation completely collapses and α^* reaches 100% again; no sign of cavitation is present further downstream. In figure 12(*b*), C_n increases to 1.05 and cavitation is much more pronounced. At the entrance, bubble cavitation can be observed. The lowest value of α^* is 90% which is still a very low void fraction.

If C_n rises to 1.15 (figure 12(*c*)), film cavitation occurs inside the cavitation channel. For this case, α^* drops down to ~65% and remains at this value up to $z = 50$ mm. Beyond that point, cavitation collapses and α^* rises again to 100% at $z = 80$ mm. In the case of film cavitation, α^* can be estimated from the photographic images by calculating the circular area

of the water core and dividing it by the circular area of the cavitation channel. However, this method cannot be used in the collapsing area or in the low cavitation cases since the vapor and liquid phases cannot be distinguished in the photographic images. Increasing the cavitation number to $C_n = 1.5$ (figure 12(*d*)) results in almost identical cavitation patterns from the entrance ($z = 0$) up to $z = 50$ mm compared to $C_n = 1.05$ (figure 12(*c*)). The only difference is that the void fraction is slightly higher in figure 12(*d*) and continuously increases up to $z = 80$ mm. A value of $\alpha^* = 100\%$ was not reached again. This implies that some cavitation structures exit the channel.
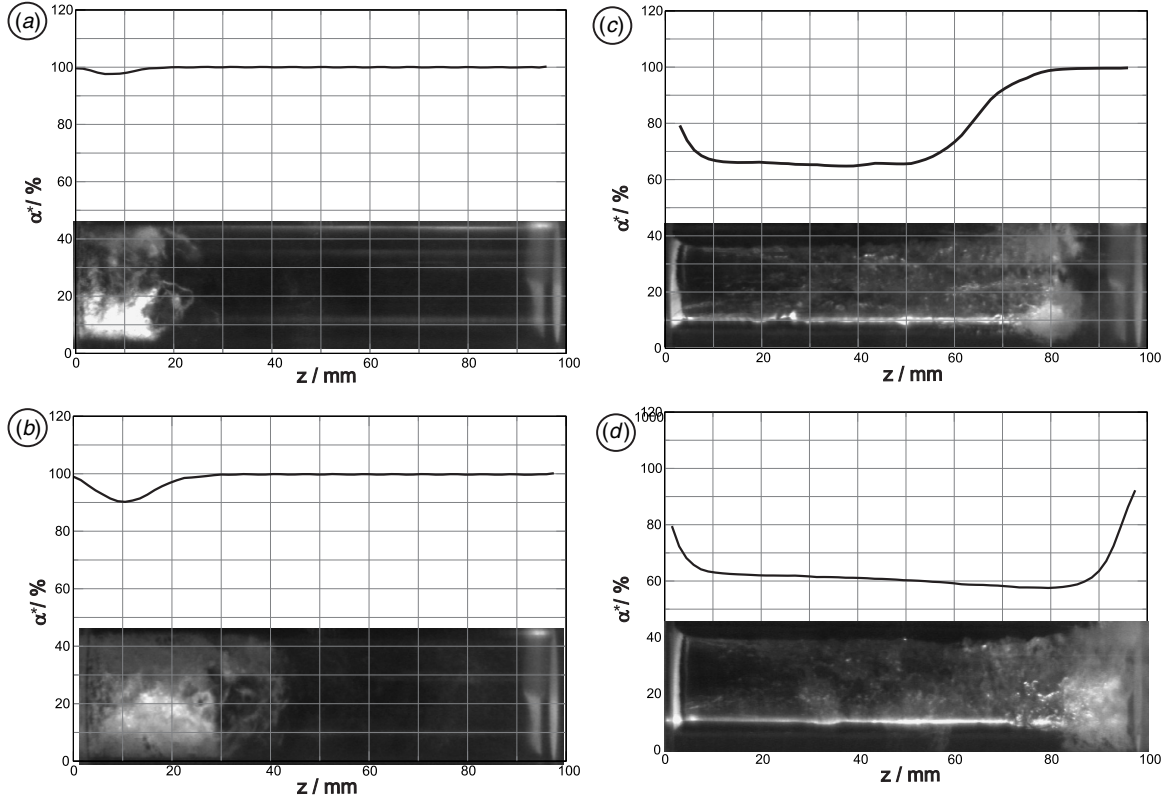
Figure 12. Spatially averaged amount of water: (a) $C_n = 0.95$, (b) $C_n = 1.05$, (c) $C_n = 1.15$, (d) $C_n = 1.5$.

Table 1. Axial positions of CT cross sections along the z-coordinate.

	(a)	(b)	(c)	(d)	(e)	(f)
z (mm)	4.25	19.25	40.25	59.75	80.75	94.25

4.4. Cross-sectional distribution of cavitation structures

In figure 13, the cross-sectional void fraction distribution for the case of $C_n = 1.5$ is depicted. The CT images were taken at the positions indicated in the photographic image below; the exact z-positions can be extracted from table 1. It should be noted that in the CT images one pixel has the dimension of $100\,\text{mm}^2$. Each image was taken within one rotation cycle of the x-ray tube. That means that with that CT system, fast phenomena like bubble break-up cannot be observed with high temporal resolution, but it is possible to locate the area where break-up occurs. In such areas, no sharp borders inside the fluid are visible. On the other hand, since the cavitation is very stable, the rotation time is sufficient to display the cavitation phenomena with longer lime scales.

Close to the entrance of the cavitation channel (figure 13(a)), cavitation is concentrated in an annulus at the sharp edge at the entrance. The size of this annulus is 2 mm. The lowest α^* at this location is 60%; however, in the core, there is pure water with no sign of cavitation.

Further downstream, cavitation has increased in strength as evidenced by the higher void fraction and the liquid has completely separated from the wall (see figure 13(b)). However, as shown in figures 13(b) and (c), the amount of liquid water in terms of α^* does not decrease to 0%, but

remains at a few percent. The reason is the presence of water droplets that leave the liquid core and enter the vapor-filled cavitation region. Another interesting observation is the shape of the cavitation area where cavitation is enhanced in radial steps of $120°$ due to the shape of the water inlet into the nozzle. It should be noted that the three inlets are set in $120°$ steps (see figure 6) which causes higher velocities and lower pressure in the cavitation channel.

Another example that demonstrates the potential of the CT can be seen in figure 13(c). With increasing z, the diameter of the liquid core is reduced and, as a result of the conservation of mass, higher flow velocity is induced. This in turn leads to a lower static pressure inside the liquid core and another cavitation region emerges which can be seen in figure 13(c) represented by the yellow circle in the center. It has no connection to the near wall cavitation area.

Within figures 13(d) and (e), it can be seen that cavitation still increases inside the liquid core. The value of α^* constantly decreases with increasing z as the cavitation structures inside the liquid core expand (see also figure 12(d)). Between the positions of figure 13(e) and (f), cavitation changes from bubble cavitation to cloud-like cavitation with film cavitation no longer identifiable.

From figure 13(f), it is clear that only cloud-like cavitation occurs at the exit of the channel. Vapor and water phase have fully mixed as can be seen from the nearly constant value of α^* across the cross section of the channel with an average void fraction of about 50%.

A cross section through the x–z-plane (at $y = 10\,\text{mm}$) of the CT images allows visualization of additional cavitation
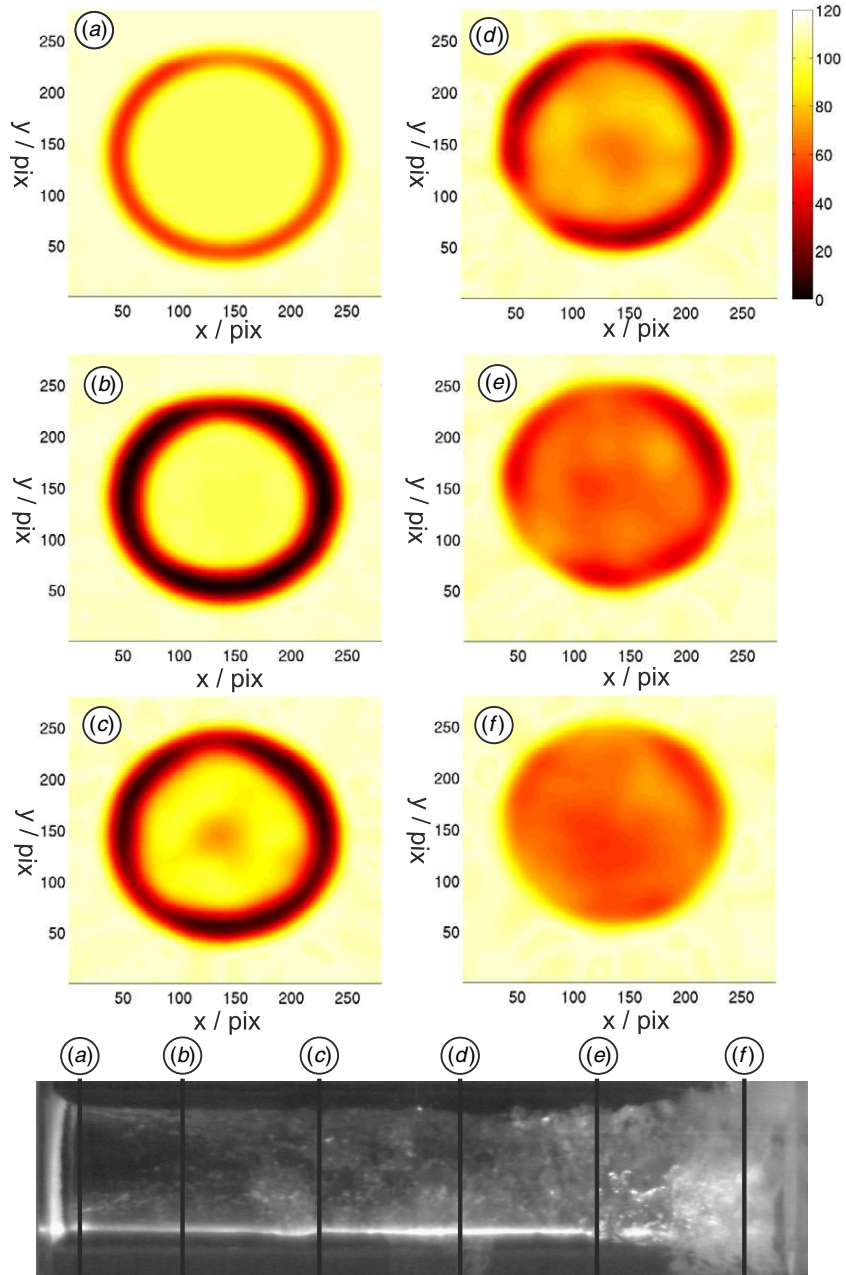
Figure 13. Cross-sectional CT images at different axial positions (see table 1) labeled from (*a*)–(*f*); $C_n = 1.5$; the color contours represent the value of α; values higher than 100 represent the solid wall made of Perspex®.
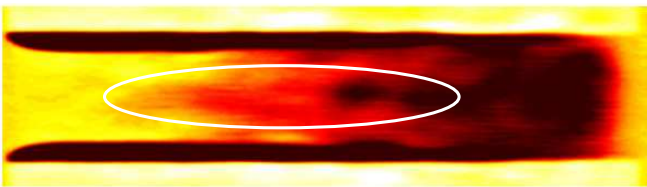

Figure 14. Cross section through the *x*–*z*-plane for $C_n = 1.5$ showing an additional cavitation zone in the center of the liquid core (ellipse).

zones in the center of the liquid core (figure 14). The beginning of the new cavitation area in the center of the core is highlighted with an ellipse, superposed on the image. The darker the color, the stronger is the cavitation and, therefore, the lower is the value of α^*. This demonstrates once more the abilities of the new measurement method.

5. Concluding remarks

In this study, the phenomenon of cavitation was investigated by CT measurements of the flow through a purpose-built nozzle. Cavitation was characterized by means of the spatial-averaged void fraction.

The results of the cross-sectional CT-measurements complemented by photographic images have allowed more detailed information about the cavitation development to be obtained. Using this technique, it has been possible to visualize

and quantify structures inside a cavitation region which are usually invisible in photographic visualization. It should be noted that, due to the time averaging over 1 second, the flow should be quasi-steady in order to identify typical regions of higher and lower cavitation. In addition, the location of the cavitation region does not influence the quality of the measurements.

Overall, the results show that x-ray computed tomography can be a very powerful tool in cavitation research, as it can be used for any quasi-steady cavitation flows irrespective of geometry, as long as the model is made from a material with an HU value slightly higher than the HU value of water.

Acknowledgments

Appendix. Parameters of all investigated cases

Table A1. Summary of all applied experimental conditions.

X^* (mm)	$\dot{V}$ (l s^{-1})	$\bar{u}$ (m s^{-1})	p_1 (mbar)	p_2 (mbar)	C_N
16	2.2	7.0	1300	962	0.35
16	2.5	8.0	1402	945	0.5
16	2.7	8.6	1469	935	0.6
16	3.0	9.6	1574	916	0.75
16	3.3	10.5	1688	903	0.9
16	3.5	11.1	1761	893	1.0
16	3.7	11.8	1860	881	1.15
16	3.8	12.1	1893	876	1.2
16	3.9	12.4	1952	862	1.35
16	4.0	12.7	2060	850	1.5
11	2.3	7.3	1335	954	0.4
11	2.6	8.3	1420	941	0.55
11	2.8	8.9	1497	927	0.65
11	3.2	10.2	1642	908	0.85
11	3.5	11.1	1761	894	1.0
11	3.8	12.1	1901	868	1.25
11	3.9	12.4	1978	869	1.35
11	4.0	12.7	2050	860	1.45
6	1.8	5.7	1247	970	0.3
6	2.3	7.3	1397	958	0.5
6	2.6	8.3	1509	942	0.65
6	2.8	8.9	1599	927	0.75
6	2.9	9.2	1627	919	0.8
6	3.1	9.9	1713	907	0.95
6	3.2	10.1	1761	907	1.0
6	3.3	10.5	1835	903	1.05
6	3.4	10.8	1879	911	1.1
6	3.5	11.1	1966	925	1.15
6	3.8	12.1	2210	916	1.5

Table A1. (Continued.)

X^* (mm)	$\dot{V}$ (l s^{-1})	$\bar{u}$ (m s^{-1})	p_1 (mbar)	p_2 (mbar)	C_N
2	1.4	4.5	1511	980	0.55
2	1.6	5.1	1709	970	0.8
2	1.8	5.7	1890	965	1.0
2	2.0	6.4	2100	964	1.25
2	2.2	7.0	2350	954	1.55
2	2.4	7.6	2600	958	1.8
2	2.7	8.6	3300	923	2.7

References

[1] Aeschlimann V, Barre S and Lagoupil S 2011 X-ray attenuation measurements in a cavitating mixing layer for instantaneous two-dimensional void ratio determination *Phys. Fluids* **23** 055101

[2] Brennen C E 1995 *Cavitation and Bubble Dynamics* (Oxford: Oxford University Press)

[3] Chaves H, Miranda R and Knake R 2007 Particle image velocimetry measurements of the cavitating flow in a real size transparent VCO nozzle *6th Int. Conf. on Multiphase Flow (ICMF 2007)*

[4] Coutier-Delgosha O, Devillers J, Pichon T, Vabre A and Woo R 2006 Internal structure and dynamics of sheet cavitation *Phys. Fluids* **18** 017103

[5] Giannadakis E, Gavaises M and Arcoumanis C 2008 Modelling of cavitation in diesel injector nozzles *J. Fluid Mech.* **616** 153–93

[6] Harada K, Murakami M and Ishii T 2006 PIV measurements for flow pattern and void fraction in cavitating flows of He II and He I *Cryogenics* **46** 648–57

[7] Lee H, Homma A, Tatsumi E and Taenaka Y 2010 Observation of cavitation pits on mechanical heart valve surfaces in an artificial heart used in in vitro testing *J. Artif. Organs* **13** 17–23

[8] Lee H and Taenaka Y 2006 Observation and quantification of cavitation on a mechanical heart valve with an electro-hydraulic total artificial heart *Int. J. Organs* **29** 303–7

[9] Miranda R, Chaves R, Martin U and Obermeier F 2003 Cavitation in a transparent real size VCO injection nozzle *Proc. ICLASS (Sorrento)* pp 199–210

[10] Radon J 1917 Über die Bestimmung von Funktionen durch ihre Integralwerte längs bestimmter Mannigfaltigkeiten *Ber. Verb. Sächs. Akad. Wiss. Leipzig, Math.-Nat.* **69** 262–77

[11] Vabre A, Gmar M, Lazaro D, Legoupil S, Coutier O, Dazin A, Lee W K and Fezzaa K 2009 Synchrotron ultra-fast x-ray imaging of a cavitating flow in a Venturi profile *Proc. 10th Int. Workshop on Radiation Imaging Detectors*

[12] Wang Y, Liu X and Lee W K *et al* 2008 Ultrafast x-ray study of dense-liquid-jet flow dynamics using structure-tracking velocimetry *Nature Phys.* **4** 305–9

[13] Wildenschild D, Vaz C M P, Rivers M L, Rikard D and Christensen B S B 2002 Using x-ray computed tomography in hydrology: systems, resolutions, and limitations *J. Hydrol.* **267** 285–97

[14] Kalender W A 2000 *Computertomographie—Grundlagen, Gerätetechnik, Bildqualität, Anwendungen* (Publicis MCD Verlag)